

## Full Length Articles

# Framework for integrated MRI average of the spinal cord white and gray matter: The MNI–Poly–AMU template



V.S. Fonov<sup>a</sup>, A. Le Troter<sup>d,e</sup>, M. Taso<sup>d,e</sup>, B. De Leener<sup>b</sup>, G. Lévêque<sup>b</sup>, M. Benhamou<sup>b</sup>, M. Sdika<sup>f</sup>, H. Benali<sup>g</sup>, P.-F. Pradat<sup>g,h</sup>, D.L. Collins<sup>a</sup>, V. Callot<sup>d,e</sup>, J. Cohen-Adad<sup>b,c,\*</sup>

<sup>a</sup> Montreal Neurological Institute (MNI), McGill University, Montreal, QC, Canada

<sup>b</sup> Institute of Biomedical Engineering, Polytechnique Montreal (Poly), Montreal, QC, Canada

<sup>c</sup> Functional Neuroimaging Unit, CRIUGM, Université de Montréal, Montreal, QC, Canada

<sup>d</sup> Centre de Résonance Magnétique Biologique et Médicale (CRMBM), UMR 7339, Aix-Marseille Université (AMU), CNRS, 13385 Marseille, France

<sup>e</sup> Centre d'Exploration Métabolique par Résonance Magnétique (CEMEREM), Hôpital de la Timone, AP-HM, 13005 Marseille, France

<sup>f</sup> Université de Lyon, CREATIS, CNRS UMR 5220, Inserm U1044, INSA-Lyon, France

<sup>g</sup> Sorbonne Universités, UPMC Univ Paris 06, INSERM, CNRS, Laboratoire d'Imagerie Biomédicale, F-75005 Paris, France

<sup>h</sup> Département des Maladies du Système Nerveux, AP-HP, Groupe Hospitalier Pitié-Salpêtrière, Paris, France

## ARTICLE INFO

## Article history:

Accepted 30 August 2014

Available online 7 September 2014

## Keywords:

Spinal cord

MRI

Template

Group analysis

Registration

## ABSTRACT

The field of spinal cord MRI is lacking a common template, as existing for the brain, which would allow extraction of multi-parametric data (diffusion-weighted, magnetization transfer, etc.) without user bias, thereby facilitating group analysis and multi-center studies. This paper describes a framework to produce an unbiased average anatomical template of the human spinal cord. The template was created by co-registering T<sub>2</sub>-weighted images (N = 16 healthy volunteers) using a series of pre-processing steps followed by non-linear registration. A white and gray matter probabilistic template was then merged to the average anatomical template, yielding the MNI–Poly–AMU template, which currently covers vertebral levels C1 to T6. New subjects can be registered to the template using a dedicated image processing pipeline. Validation was conducted on 16 additional subjects by comparing an automatic template-based segmentation and manual segmentation, yielding a median Dice coefficient of 0.89. The registration pipeline is rapid (~15 min), automatic after one C2/C3 landmark manual identification, and robust, thereby reducing subjective variability and bias associated with manual segmentation. The template can notably be used for measurements of spinal cord cross-sectional area, voxel-based morphometry, identification of anatomical features (e.g., vertebral levels, white and gray matter location) and unbiased extraction of multi-parametric data.

© 2014 Elsevier Inc. All rights reserved.

## Introduction

Magnetic resonance imaging (MRI) of the spinal cord has tremendous potential for improving diagnosis/prognosis in traumatic, inflammatory and other causes of diseases, as well as for evaluating the effect of new drugs. In particular, multi-parametric MRI, combining several quantitative techniques (e.g., diffusion-weighted imaging, magnetization transfer, functional MRI) provides a variety of biomarkers sensitive to white matter damage and neuronal function in the spinal cord (Wheeler-Kingshott et al., 2014; Cohen-Adad et al., 2011a; Stroman et al., 2014). However, spinal cord MRI faces two major challenges: data acquisition and data processing. Although recent developments in phased-array coils (Cohen-Adad et al., 2011b), and pulse

sequences (Dowell et al., 2009; Finsterbusch et al., 2012) help overcome the numerous artifacts associated with spinal cord imaging, only modest efforts were directed towards the development of publicly-available processing tools dedicated to spinal cord MRI data.

In particular, the lack of a common template makes it difficult to process multi-parametric data within a standard framework, because extraction of metrics requires the user to manually draw binary regions of interests (ROIs) based on the perception of the underlying anatomy (e.g., location of the spinal cord gray matter or corticospinal tract). These approaches are subject to inter- and intra-rater variability and bias, and cannot easily be ported to large-scale studies. A template is an image of a given structure averaged across multiple individuals, and used as a frame of reference for image registration and atlas-based MR signal quantification. For example, the introduction of common MRI brain templates (e.g., the MNI template) (Collins et al., 1994) revolutionized neuroimaging by enabling group analysis and allowing researchers to share, compare and validate their results. With brain templates, extraction of metrics within specific areas (e.g., motor

\* Corresponding author at: Institute of Biomedical Engineering, Polytechnique Montreal, Campus Université de Montréal, 2900 Edouard-Montpetit Bld, Montreal, QC H3T1J4, Canada. Fax: +1 514 340 4611.

E-mail address: [jcohen@polymtl.ca](mailto:jcohen@polymtl.ca) (J. Cohen-Adad).

cortex) can be computed, providing a robust and objective analytical framework. Currently no such template exists for spinal cord, de facto preventing researchers and clinicians to systematically and robustly study the association between structure and function in the healthy spinal cord, or microstructural damages in the spinal cord and clinical symptoms for example.

Some groups have tackled this issue by creating templates specific to their research experiments. Stroman et al. created a template from  $1 \times 1 \times 2 \text{ mm}^3$  T<sub>2</sub>-weighted (T<sub>2</sub>w) fast spin echo data of 8 subjects for application in functional MRI (Stroman et al., 2008). They manually delineated the anterior edge of the spinal cord from the caudal edge of the pons to the C7/T1 intervertebral disk to straighten the cord, then performed a stretching/compression of each individual cord to register them together. They later used an absolute distance from the pontomedullary junction (Stroman et al., 2012), in order to obtain a more accurate representation of the spinal level—as opposed to the vertebral level—as supported by anatomical studies (Lang, 1993). One limitation of this approach is the need to manually identify the edge along the cord. Later, Valsasina et al. proposed a normalization procedure, which consists of segmenting the cord using a semi-automated method (Horsfield et al., 2010) and then registering the cords using manually-identified landmarks at C1 and C7 vertebral levels (Valsasina et al., 2012). The authors applied this method for voxel-based morphometry analysis and demonstrated its sensitivity for detecting significant changes of cord tissue with aging. A limitation inherent to the two previously-cited methods is the absence of a single deformation (warping field) that registers the anatomical data of a given subject to the template, and that is bijective (i.e., enables forward and backward transformation). Such a warping field would be useful for registering multi-parametric data to a common space for subsequent quantification of image-derived metrics. This approach is commonly used by standard brain processing pipelines (e.g., SPM, FSL, AFNI, MinTools). Another study introduced a method for creating a spinal cord template from axial T<sub>2</sub>w images (Tozer et al., 2012). In their framework, the authors: (i) cropped the data around the cord, (ii) performed an affine intra-subject registration with FLIRT (Jenkinson et al., 2002), (iii) non-linearly registered the data across subjects with FNIRT (part of FSL) and (iv) averaged all registered data. One limitation of this approach is that a subject has to be arbitrarily selected as the reference for non-linear registration, which introduces bias towards a specific anatomy in the final template. In another study by Eippert et al., the authors created a template by using the normalization algorithms from SPM (including both affine and non-linear terms) to register T<sub>1</sub>w images from 15 healthy subjects (Eippert et al., 2009). Again here, one subject was selected as the reference subject. Another recent development proposed a framework for creating a generic template of the spinal cord (Chen et al., 2013). This approach however is based on the generation of a study-specific template (which notably depends on a particular image contrast)—yet, it would be beneficial to develop a universal template for comparing studies across groups. An additional limitation shared by all previous attempts was that the generated templates were not readily accessible to the community.

In light of the previous developments, there is a need for a processing pipeline to create a template of the spinal cord and to register new subjects to it, with the following conditions: (i) to generate the template, no subject should be arbitrarily selected as the reference subject, (ii) the registration procedure should be based on a bijective deformation that is estimated using a robust and automatic procedure suitable for large-scale studies, (iii) the template creation and registration pipeline should be based on platform-independent and freely available software and scripting environment and (iv) the template itself should be freely available.

In addition to the generation of a common template, it would be useful to be able to obtain morphological measures of the spinal cord gray matter. For example, measuring the gray matter cross-sectional area (CSA) at a given spinal level would improve the specificity over the

whole spinal cord CSA measure in motor-neuron diseases such as amyotrophic lateral sclerosis. Identifying the cord gray matter would also be useful for interpreting functional MRI results. Although segmenting the spinal cord gray matter has always been a challenge due to its small size and lack of contrast in most sequences, some groups have recently showed the feasibility to segment the gray matter using manual (Sigmund et al., 2012; Taso et al., 2014b; Yiannakas et al., 2012) and automatic (Asman et al., 2014) methods. Hence, an additional useful feature for the generation of a common spinal cord template would be the integration of a probabilistic gray matter (and white matter) atlas. This atlas could be used to initialize label fusion segmentation methods (Asman et al., 2014) or to study gray matter morphology (Fradet et al., 2014). A white and gray matter probabilistic atlas of the spinal cord was recently developed (Taso et al., 2014b), and is an ideal candidate for integration into a new common spinal cord template.

The aims of this study were to (i) create an unbiased symmetric T<sub>2</sub>w template of the human spinal cord, (ii) merge the created template with an existing probabilistic gray and white matter atlas (Taso et al., 2014b) and (iii) propose a semi-automatic pipeline to register new subjects to the template. The **Material and methods** section details the pre-processing and registration steps to generate the T<sub>2</sub>w template, integration with the probabilistic atlas and the pipeline is validated against manual segmentations. The **Results** section presents the new template and atlas, the validation of registration to the template, measures of CSA along the spinal cord and shows an example of multi-modal registration. The **Discussion** section addresses limitations, applications and future works.

## Material and methods

### MRI acquisition

This section describes the acquisition protocol used for collecting data used for (i) creating the T<sub>2</sub>-weighted template, (ii) creating the gray/white matter probabilistic template and (iii) validating the registration pipeline. Note that these three acquisition protocols used different groups of subjects and different scanners.

### Data for T<sub>2</sub> template creation

To create the spinal cord T<sub>2</sub> template, 16 subjects were recruited (mean age:  $26 \pm 3$  y.o., 7 men and 9 women). Data were acquired on a 3 T MRI system (TIM Trio, Siemens Healthcare, Erlangen, Germany) at the Pitié-Salpêtrière Hospital (Paris, France). The local ethics committee approved all experimental procedures and written informed consent was obtained from each participant. The body coil was used for excitation and signal reception was achieved using a combination of 12-channel head-coil, 4-channel neck coil and a 24-channel spine matrix array.

The imaging protocol included a T<sub>2</sub>-weighted 3D fast spin echo (FSE) with slab selective excitation sequence with the following parameters: sagittal orientation, one slab of 52 slices, field of view (FOV) = 280 mm, TR = 1500 ms, TE = 120 ms, voxel size =  $0.9 \times 0.9 \times 0.9 \text{ mm}^3$ , flip angle = 140°, parallel acquisition with R = 3 (GRAPPA reconstruction), phase encoding direction head-foot, phase oversampling 80%, slice oversampling 7.7%, bandwidth = 744 Hz/pixel, turbo factor = 69, acquisition time 6 min.

### Data for gray/white matter probabilistic template

To create the gray/white matter probabilistic template, 15 other subjects were used (mean age:  $27 \pm 5$  y.o., 9 men and 6 women) as part of an already-published study (Taso et al., 2014b). Data were acquired on a 3 T MRI system (Verio, Siemens Healthcare, Erlangen, Germany) at the CEMEREM, La Timone Hospital (Marseille, France). The local ethics committee approved all experimental procedures and written informed consent was obtained from each participant. The body coil was used for excitation and signal reception was achieved using a combination

of 12-channel head-coil, 4-channel neck coil, 24-channel spine matrix array and flexible 6-channel body coil for thoracic and lumbar levels.

The imaging protocol included a multi-echo gradient echo sequence with the following parameters: axial orientation (each slab perpendicular to the spinal cord), five echoes, effective TE = 27 ms, flip angle = 28°, FOV = 180 × 135 mm<sup>2</sup>, in-plane resolution 0.46 × 0.46 mm<sup>2</sup>, 2 slabs (C1–C7, T1–T7) of seven non-contiguous transverse slices (one slice per vertebral level), slice thickness 5 mm, ECG synchronization (trigger delay 300 ms), parallel acquisition with R = 2 (GRAPPA reconstruction) and three signal averages.

#### Data for validation

Validation was assessed from additional 16 healthy subjects (mean age: 25 ± 6 y.o., 6 men and 10 women). These subjects were different from the subjects used to produce the T<sub>2</sub> template and the gray/white matter template. In order to remove biases associated with scanning at the same institution (e.g., patient handling, sequence parameters, scanner), these subjects were scanned at another institution (Functional Neuroimaging Unit, CRIUGM, Université de Montréal, Montreal, Canada). Data were acquired on a 3 T MRI system (TIM Trio, Siemens Healthcare, Erlangen, Germany) using the commercial 12-channel head-coil, 4-channel neck coil and a 24-channel spine matrix array.

Sequence used for registration to the template was a T<sub>2</sub>-weighted 3D FSE, sagittal orientation, 52 slices, FOV = 384 mm, voxel size = 1 × 1 × 1 mm<sup>3</sup>, TR = 1500 ms, TE = 119 ms, flip angle = 140°, bandwidth = 723 Hz/pixel, and parallel acquisition with R = 3 (GRAPPA reconstruction).

To illustrate the feasibility to register images with other contrasts and resolution, additional sequences were run on a subject (M, 23 y.o.). These included (i) a T<sub>1</sub>-weighted multi-echo MPRAGE (TR = 8.6 ms, TE = {2,4,5,8}ms, flip angle = 20°, FOV = 264 × 384 mm<sup>2</sup>, 176 slices, 1 × 1 × 1 mm<sup>3</sup>), (ii) a 2D gradient echo sequence with magnetization transfer (MT) pulse (TR/TE = 600/4.83 ms, flip angle = 25°, FOV = 162 × 162 mm<sup>2</sup>, 5 slices, 0.8 × 0.8 × 5 mm<sup>3</sup>, Gaussian MT pulse), (iii) diffusion-weighted EPI with 2DRF excitation (Finsterbusch, 2009) (TR ~ 2200 ms with pulse-oxymeter cardiac gating, TE = 87 ms, FOV = 175 × 35 mm<sup>2</sup>, 0.8 × 0.8 × 5 mm<sup>3</sup>, bandwidth = 925 Hz/pixel, 24 diffusion-encoding directions, b = 800 s/mm<sup>2</sup>), and (iv) T<sub>2</sub>\*-weighted EPI (TR/TE = 1130/26 ms, flip angle = 90°, FOV = 65 × 65 mm<sup>2</sup>, 1 × 1 × 3 mm<sup>3</sup>, bandwidth = 1021 Hz/pixel, 20 repetitions).

#### Image pre-processing

T<sub>2</sub>-weighted image pre-processing on each subject consisted of the following steps:

1. Image denoising using adaptive non-local means (Manjon et al., 2010). This filter uses a blockwise approach in comparison with the standard voxel-based non-local means algorithm, and also takes into account both the Rician nature of the MR data and the spatially varying noise patterns introduced by multichannel array coils and parallel imaging reconstruction.
2. Intensity non-uniformity correction using N4ITK (Tustison et al., 2010). This filter uses a fast and robust B-spline approximation routine and a modified hierarchical optimization scheme for improved bias field correction over the original non-parametric non-uniform intensity normalization (N3) algorithm. The following parameters were used: spline distance 100 mm (length of a B-spline mesh element), shrink factor 2 (image downsampling), convergence threshold 0.001, maximum number of iterations 100 (maximum iteration was reached every time).
3. Approximate spinal canal segmentation and spinal cord straightening using the following procedure:
  - a Manual identification of the center of spinal cord corresponding to the vertebral disk between C2 and C3. This is the only manual step required, all other processing steps are automated.

- b Segmentation of the spinal canal (spinal cord and CSF) on a single 2D axial slice is achieved using a graph-cut image segmentation algorithm (Boykov and Funka-Lea, 2006), where the pixel at the center of the spinal cord identified in step (a) is used as an “S” node (foreground) and all pixels located further than 20 mm from the center are set to be “T” nodes (background). Using Eq. (1) to set asymmetric capacities of the links between adjacent pixels *a* and *b*:

$$W_{a,b} = \frac{1}{\text{dist}(a,b)} \begin{cases} \exp\left(-\frac{(I_a - I_b)^2}{2\delta^2}\right), & I_a < I_b \\ 1, & I_a \geq I_b \end{cases} \quad (1)$$

where *I<sub>a</sub>* is the intensity of pixel *a*; *I<sub>b</sub>* is the intensity of pixel *b*; *dist(a, b)* is the geometrical distance between pixels *a* and *b*, here pixels immediately adjacent to each other receive distance of 1 and diagonally adjacent ones receive distance  $\sqrt{2}$ ; and  $\delta$  is the smoothing coefficient estimated using median absolute deviation (Huber and Ronchetti, 2009) of the gradient magnitudes within the slice.

- c In order to estimate the spinal cord center of the next adjacent axial slice (*z* + 1), both slices are co-registered using cross-correlation cost function and 3 parameter transformation (shift in *x*, *y* and *z*-rotations). To increase robustness, the transformation is estimated within the mask of the spinal canal identified at step (b). Linear registration is performed using the hierarchical registration framework implemented in ITK as *MultiResolutionImageRegistrationMethod* and *RegularStepGradientDescentOptimizer*. Note that *z*-rotations are not problematic because the goal of this step is only to estimate the spinal cord centerline (single point per slice), not the in-plane orientation of the cord.
- d Iterate through consecutive slices by repeating steps b and c until the most inferior and the most superior axial slices are reached, producing an estimation of the location of the center of spinal cord for each slice: *X(z)*, *Y(z)*
- e Resulting per-slice segmentations of the spinal canal are then used to calculate median per-slice intensity in the spinal cord *I(z)*
- f Gaussian smoothing is applied to *X(z)*, *Y(z)* and *I(z)* with  $\sigma = 8$  mm (chosen empirically based on preliminary results).
- g Dense non-linear transformation fields are calculated by mapping extracted centers of the spinal cord to a straight vertical line (spinal cord straightening). The interface between C2 and C3 is manually identified, then landmarks are automatically generated as follows: one in the center of the spinal canal and four more in the slice perpendicular to the detected centerline. These landmarks are created for each slice. A non-linear transformation is then calculated between the curved landmarks and the straight landmarks. The transformation is represented as thin-plate splines, as implemented in ITK as *LandmarkDisplacementFieldSource*.
- h A second intensity-inhomogeneity correction is performed by linearly normalizing intensities of slices based on *I(z)*. The reason for doing this step in addition to the N4ITK (step 2) is that here, the intensity is normalized based on the mean intensity within the spinal cord (per slice), whereas the N4ITK filter was applied to the whole image.
- i The overall intensity range is linearly scaled so that mean intensity within the spinal canal is 1000. This value was chosen arbitrarily.
- j The resulting intensity-normalized image volume was resampled into a common space on a 0.5 × 0.5 × 0.5 mm voxel grid, using 2nd order B-spline interpolation, applying non-linear transformation calculated at step (g).

#### Template creation

##### Creation of the T<sub>2</sub> spinal cord template (MINI-Poly)

An unbiased left–right symmetric spinal cord template was constructed using hierarchical group-wise image-registration method described in Fonov et al. (2011) by using results of the image-



preprocessing steps described in the [Image pre-processing](#) section as input to the template creation process. This method is based on the non-linear registration engine of Automatic Nonlinear Image Matching and Anatomical Labeling (ANIMAL) (Collins et al., 1995). The overall steps are to perform nonlinear registration of each subject's spinal canal into an average space, and repeat the procedure several times using finer grid step size and blurring kernel. The following hierarchical schedule was used: 4 iterations at 16 mm resolution, 4 iterations at 8 mm, 4 iterations at 4 mm, 4 iterations at 2 mm and 8 iterations at 1 mm. After the final iteration, and in order to obtain a straight spinal cord, the center of mass of the spinal cord was calculated at each slice and then mapped to fit a straight vertical line (as in step 3.g found in the [Image pre-processing](#) section). The resulting template was centered in the antero-posterior and in the right-left direction in order to have the spinal cord centered in the middle of the volume. The final resolution of the template was set to  $0.5 \times 0.5 \times 0.5 \text{ mm}^3$  for a size of  $120 \times 120 \times 600$  voxels.

Masks and labels associated with the average template were created from the average of the graph cut segmentation: mask and boundaries of the spinal cord, mask of the CSF, boundaries between the CSF and the spine, label of vertebral level (incremental value, starting at mid-C1 and ending at T6).

The ensemble of the T<sub>2</sub>-template, masks and labels forms the *Montreal Neurological Institute-Polytechnique Montreal* (MNI-Poly) T<sub>2</sub> template.

#### Creation of the white and gray matter probabilistic template (AMU)

The white matter (WM)/gray matter (GM) probabilistic template used here was previously created by Taso et al. (2014b) using gradient echo images acquired in 15 subjects (see the [Data for gray/white matter probabilistic template section](#)) and is referred to as the *Aix-Marseille University* (AMU) template. Each voxel of the AMU template represents the proportion of subjects with that tissue label (white or gray matter) at that voxel position. Since the AMU template contains one slice per vertebral level from C1 to T12, it must be resampled into a 3D volume for proper fusion with the average MNI-Poly T<sub>2</sub> template created in the [Creation of the T<sub>2</sub> spinal cord template \(MNI-Poly\) section](#). Resampling the AMU template was done as follows:

1. The 2D native AMU template slices were resampled from  $0.46 \times 0.46 \text{ mm}$  in-plane sampling to  $0.5 \text{ mm}$  isotropic sampling so as to match the spatial resolution of the MNI-Poly T<sub>2</sub> template.
2. Since the MNI-Poly T<sub>2</sub> template is left-right symmetric, the AMU template must be made symmetric as well. The 2D native AMU template slice images were centered in the AP and RL directions. Symmetrized images were thus obtained by flipping the native images in the RL direction and by averaging the flipped and non-flipped images.
3. In order to match the superior-inferior slice spacing of the MNI-Poly T<sub>2</sub> template ( $0.5 \text{ mm}$ ), it was necessary to interpolate slices between the AMU template images. This was achieved with pairwise linear interpolation to create a 3D isotropic volume.

#### Fusion between the MNI-Poly and the AMU templates

After resampling the AMU template into the voxel grid of the MNI-Poly T<sub>2</sub> template, it is still necessary to register the two datasets so that anatomical features are aligned. Co-registration between MNI-Poly and AMU templates first involved two scaling factors in the x and y directions (i.e., no z-translation or rotations were considered given the R-L symmetric nature of the MNI-Poly T<sub>2</sub> and AMU templates). The transformation was estimated slice-wise using regularization constraints along z (smoothing of scaling factors along z). A second step consisted of non-linear co-registration using ANTs (Avants et al., 2008). Parameters were: SyN transformation (symmetric image normalization method for estimating diffeomorphic functions),  $0.2 \text{ mm}$  gradient step (characterizes the gradient descent optimization), mutual information metric, constrained in the x-y plane,  $100 \times 100$  iterations (i.e., 100

iterations at each level, with a total of two levels) using  $2 \times 1$  shrink factor (upsampling of the image at each level) and  $1 \times 0 \text{ mm}$  smoothing. The ensemble comprising the integrated MNI-Poly T<sub>2</sub> and AMU templates forms the MNI-Poly-AMU template (see [Fig. 2](#)).

#### Framework for registering new data to the template

The goal of this procedure is to register a new subject to the template and to warp template objects (spinal cord segmentations, white/gray matter maps, etc.) into the subject's native space. This is achieved using the following steps:

1. Pre-processing of subject's anatomical image as described previously in the [Image pre-processing section](#): denoising, intensity inhomogeneity correction and straightening.
2. After pre-processing, the resulting spine volume is non-linearly registered to the MNI-Poly-AMU T<sub>2</sub> template using ANTs with cross-correlation cost function, with the following parameters: cross-correlation cost function with radius of 2; Gaussian regularization of gradient field  $\sigma = 4$  and deformation field sigma = 1, SyN transformation model with gradient step length of  $0.125$  and number of time-steps 4 and number of iterations:  $200 \times 200 \times 200 \times 100$ .
3. Warping of the segmentation priors (spinal cord, CSF and white/gray matter masks, vertebral labeling) back into the native space of the subject, by concatenating the straightening deformation field calculated as part of pre-processing and the non-linear transformation field calculated at the previous step.

The output of the registration pipeline is a series of 3D volumes representing segmentation of spinal cord and CSF, probabilistic maps of white and gray matter and labeling of vertebral levels. These segmented structures can be used as ROIs for multi-parametric MRI techniques (e.g., diffusion imaging, magnetization transfer, functional MRI). Along with these volumes are the forward and backward warping fields, which can register data from and to the template, respectively.

To provide maximum flexibility for the user to integrate the pipeline into his/her environment, we propose two versions of the pipeline: pipeline #1 is based on the MINC file format using the Minc Tool Kit<sup>1</sup> and pipeline #2 is based on NIFTI file format using Python<sup>2</sup> scripts and FSL<sup>3</sup> software and is part of the Spinal Cord Toolbox (Cohen-Adad et al., 2014a). Both pipelines use ANTs<sup>4</sup> for registration.

#### Calculation of CSA by improving local deformation with graph cuts

Following registration to the template, the pipeline also produces continuous measurements of the axial spinal cord area (CSA). This is achieved by further improving the spinal cord segmentation using graph cuts as described below:

1. A discrete parametric curve describing the center of the spinal cord of the MNI-Poly-AMU is warped to the subject's native space using non-linear transformation defined above. The curve is a series of points  $(x,y,z,t)$  where  $x,y,z$  are spatial coordinates and  $t$  is a parametric coordinate along the spinal cord. These points are equally spaced in the template space along the spinal cord, but then warped to match the subject so they are not equally spaced anymore.
2. 3D Gaussian smoothing with FWHM kernel of  $0.5 \text{ mm}$  is applied to reduce aliasing artifacts. For each point on the curve (at  $0.5 \text{ mm}$  intervals) a slice perpendicular to the curve is extracted from the subject's T<sub>2</sub> scan using 2nd order B-spline interpolation with an in-plane resolution of  $0.2 \text{ mm}$ .
3. Extracted slices are stacked together as a 3D volume and a graph-cut segmentation is performed to refine spinal cord segmentation

<sup>1</sup> <http://www.bic.mni.mcgill.ca/ServicesSoftware/MINC>.

<sup>2</sup> <https://www.python.org/>.

<sup>3</sup> <http://fsl.fmrib.ox.ac.uk/fsl/fslwiki/>.

<sup>4</sup> <http://sourceforge.net/projects/advants/>.

results. The implementation is similar to that one described in the [Image pre-processing](#) section found in step 3.b, with the difference that comparison signs are inverted ( $I_a > I_b$ ), so that graph-cut segmentation procedure will find the edge corresponding to the transition from the darker (spinal cord) pixels to brighter ones (CSF).

4. After graph-cut segmentation the CSA of the spinal cord is calculated by counting pixels in the cord and multiplying by the voxel area.

Note that since this procedure does not produce warping field (only local non-bijective deformations are estimated), it is currently not possible to estimate an inverse warping field and concatenate it with the output of the [Framework for registering new data to the template section](#). This will be part of future investigations. Also note that currently the procedure is optimized for  $T_2$ -weighted images, but can easily be adapted to  $T_1$ -weighted images with inversion recovery preparation (e.g., MPAGE sequence, yielding inverted contrast between spinal cord and CSF) by inverting the comparison sign of Eq. (1) on the graph-cut segmentation.

#### Validating registration of anatomical data to the template

The registration pipeline described above was applied to the validation data (see the [Data for validation](#) section). To validate registration to the template, the spinal cord of each subject was semi-manually segmented on the 3D  $T_2$ -weighted sequence, between C1 and T3 vertebral levels. Segmentation was done with Osirix<sup>5</sup> on 12 slices (one per vertebral level), and then the parametric ROIs (2D parametric spline curves representing the contour of the spinal cord) were interpolated across slices to generate 3D ROIs in voxel space. This approach is justified by the small variation of spinal cord cross sectional shape between two vertebral levels. However, this approach can minimize the difference between the manual and the semi-automatic approach and thus does not make a fair comparison for the 3D Dice calculation. To check the validity of this approach, manual segmentations were performed on three random subjects from C1 to T3, without any interpolation (about 160 slices per subject). The 3D Dice coefficient was computed between the semi-manual ROI and the manual ROI. Results gave 3D Dice of 0.994, 0.985 and 0.997 for each subject respectively, suggesting that the semi-manual approach is an acceptable ground truth for assessing registration accuracy with the template. The semi-manual segmentations from the validation data (15 subjects) were then used to calculate following metrics describing goodness of the spine cross-section measurement:

- Differences between the spinal cord cross-section areas, for each perpendicular slice along the length of the cord from C1 to T3.
- 3D Dice Kappa overlap coefficient ([Dice, 1945](#)), comparing the manually-segmented cord and the template-based segmentation warped to the native space of the subject's anatomical data.
- 2D Dice Kappa overlap coefficient calculated at each slice perpendicular to the extracted spinal cord.
- Distances between centers of mass for each perpendicular slice along the length of the cord from C1 to T3.

To illustrate the feasibility to warp template objects on an image with different contrasts than the  $T_2$  anatomical data and acquired with non-isotropic resolution, the template was registered to the following other sequences in one subject (here we call them multi-parametric data): a 3D  $T_1$ -weighted MPAGE, an axial MT-weighted gradient echo, an axial diffusion-weighted sequence (mean diffusion weighted image was used for registration) and an axial  $T_2^*$ -weighted EPI sequence typically used for fMRI (the average of 20 volumes was used for registration). See the [Data for validation section](#) for sequence details. In order to produce robust and accurate registration between the template and the multi-parametric data, the template registered to the  $T_2$

anatomical data of the subject served as an intermediate step. Hence, the registration consisted of the following two-step approach:

1. The  $T_2$  template was registered to the  $T_2$  anatomical data using the pipeline described above. The outputs were the  $T_2$  template in the anatomical space (*template2anat*) and the associated warping field (*warp\_template2anat*).
2. The image *template2anat* was registered to each contrast using ANTs (SyN deformation, mutual information, constrained in z), producing the  $T_2$  template in each contrast native space (*template2data*) and the associated warping field (*warp\_anat2data*). The deformation fields from this step and from the previous step were then concatenated to produce the global deformation *warp\_template2data* (and its inverse, *warp\_data2template*) that warps any template object (e.g., spinal cord segmentation, white matter atlas) to and from the multi-parametric data, respectively.

## Results

[Fig. 1](#) shows the MNI-Poly  $T_2$  template with overlay of the vertebral labeling. The spinal cord is straightened with respect to its centerline and is symmetric in the L–R direction. The signal intensity was normalized within the spinal cord and within the CSF. Note that the straightening process involving thin plate splines (i.e., similar to the bending of a structure) ensured consistency in the rostro-caudal structure of the spinal cord, which can be qualitatively assessed by the quasi-perpendicular intervertebral disks with respect to the spinal cord.

[Fig. 2](#) shows the fusion between the MNI-Poly and the AMU template. The white and gray matter templates are probabilistic, i.e., their value between 0 and 1 represents the proportion of subjects with that tissue label at that voxel position. This information can be useful to weight metrics extraction in the white matter from diffusion-weighted or MTR protocols, for weighting statistical results in the gray matter for fMRI protocols or for initializing gray matter segmentation algorithms (see the [Discussion](#) section).

[Fig. 3](#) illustrates the various steps for registering new subjects to the template. First, the user defines a single voxel within the spinal cord center at the C2–C3 level (this procedure takes less than a minute). Then, the spinal cord centerline is automatically identified, followed by a straightening of the spinal cord, a rough linear registration to the template followed by a finer deformation using non-rigid transformation (ANTs SyN). All transformations are then concatenated into a single forward and a single backward transformation, which can be applied conveniently to any data from the template space or from the native space. The whole registration pipeline takes about 15 min to run (Intel i7 quad-core 3.4 GHz, 8 GB RAM).

[Fig. 4](#) shows segmentation results in the fifteen subjects used for validation. Visual inspection suggests good registration between the template and the anatomical  $T_2$  volume for all subjects, in terms of local boundary matching (spinal cord/CSF interface) and vertebral level matching. 3D Dice coefficient assessing overlap between manual segmentation and registration-based segmentation (before graph-cut segmentation) ranged within [0.76–0.88] (mean:  $0.84 \pm 0.03$ ) for pipeline #1 and [0.80–0.88] (mean:  $0.83 \pm 0.03$ ) for pipeline #2. These values were calculated for the 15 subjects from C1 to T3 vertebral levels.

[Figs. 5, 6 and 7](#) show a more detailed analysis of pipeline #1, per vertebral level. Analysis was done between C1 and T3 (because T4–T6 levels were not fully covered in some subjects). [Fig. 5](#) shows the difference between the spinal cord CSA estimated from registration and from manual segmentation. Results are shown after non-linear registration (ANTs, intermediate step) and after graph-cut segmentation (GC, final step). The GC segmentation further improved the quality of CSA estimation, reducing the average CSA area difference across vertebral levels from  $-13.9 \text{ mm}^2$  (ANTs alone) to  $-7.0 \text{ mm}^2$  (ANTs + GC). CSA was underestimated by 16%, which could be attributed to the slightly darker contour of the  $T_2$ -weighted image, accentuating partial volume effects

<sup>5</sup> [www.osirix-viewer.com](http://www.osirix-viewer.com).



**Fig. 1.** MNI-Poly T<sub>2</sub>-weighted template with vertebral labeling. Panel on the right shows axial views across vertebral levels, with overlay of spinal cord and CSF contours (vertebral levels from C1 to T5 are displayed from left to right, then top to bottom).

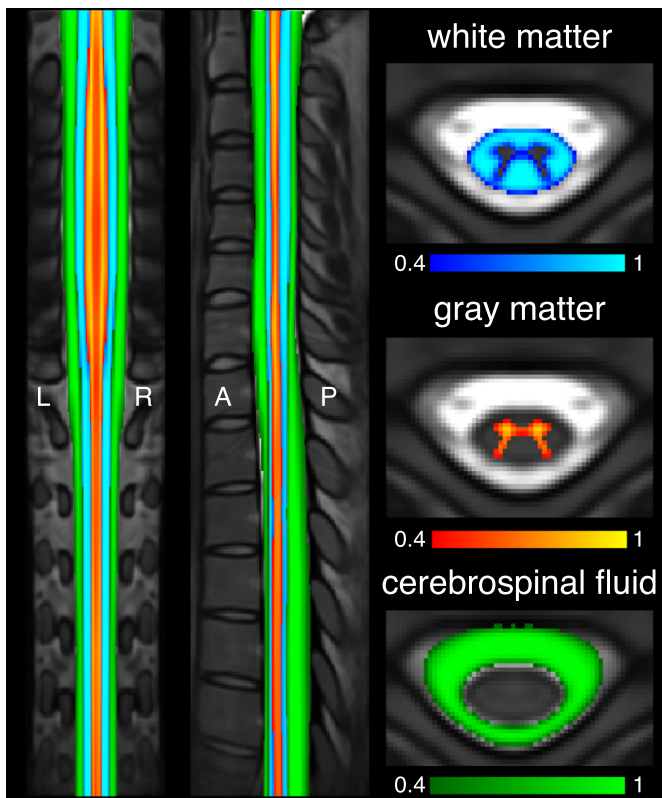


**Fig. 2.** Fusion between the MNI-Poly template and the AMU white and gray matter probabilistic map. This ensemble forms the MNI-Poly-AMU template. The axial view corresponds to C7 vertebral level.

with the surrounding CSF (see the [Discussion](#) section). [Fig. 6](#) shows the 2D Dice coefficient between the manual and the automatic segmentation. The Dice coefficient was calculated for each slice and then averaged within each vertebral level. The median Dice coefficient was 0.85 (ANTs alone) and 0.89 (ANTs + GC) and 5–95 percentiles were [0.77–0.92] (ANTs alone) and [0.82–0.94] (ANTs + GC), suggesting good overlap between the manual and the automatic segmentation for all vertebral levels. [Fig. 7](#) shows the absolute in-plane distance between center-of-mass of the spinal cord segmentation from registration and from manual results. Average Pythagorean distance between the manual and estimated center of mass was  $0.37 \pm 0.24$  mm (ANTs alone) and  $0.24 \pm 0.18$  mm (ANTs + GC), suggesting low registration error (less than 0.5 mm for all vertebral levels).

[Fig. 8](#) illustrates the outputs provided by the registration: spinal cord centerline, vertebral labeling, binary mask of the spinal cord, probabilistic masks of the white and gray matter, binary mask of the CSF with spinal cord and continuous measurements of CSA along the spinal cord. Here the centerline is represented as a binary mask but it is also accessible as a parametric spline function. The CSA is calculated from the fine-segmentation of the spinal cord, after non-linear registration of the anatomical data to the template. Note that the apparent gray matter voxels outside the spinal cord are simply due to partial volume effect—in fact, the probabilistic values of gray matter voxels outside the spinal cord are typically less than 0.1.

[Fig. 9](#) shows the registration between the template and multi-parametric data acquired with different sequences: T<sub>1</sub>-weighted MPRAGE, T<sub>2</sub>-weighted FSE, MT-weighted gradient echo, diffusion-weighted EPI (mean DWI was used for registration), T<sub>2</sub>\*-weighted EPI (mean EPI was used for registration). The template was first registered to the T<sub>2</sub> anatomical data of the subject, and then registered to each multi-parametric data using non-rigid deformation constrained in the axial plane (non-rigid deformation was necessary due to the



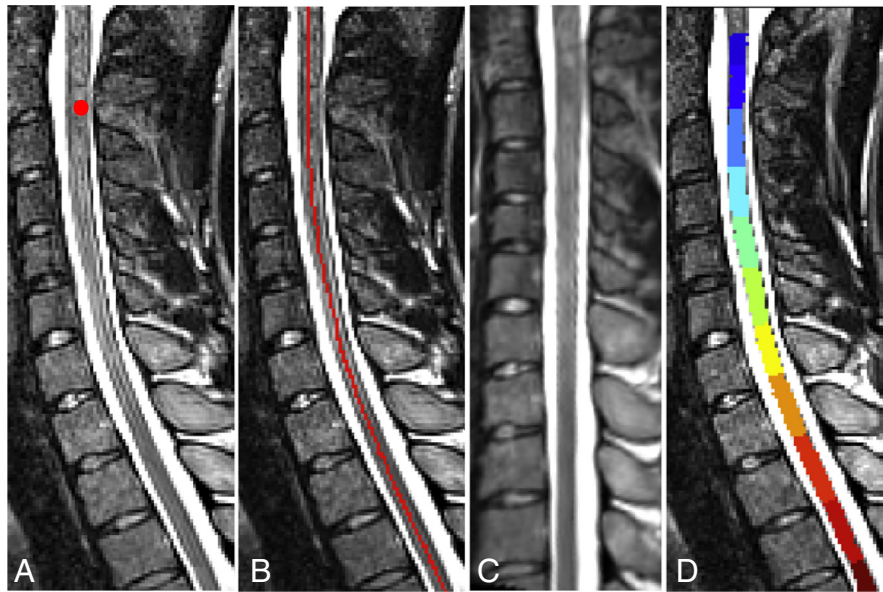


**Fig. 3.** Steps for registering a subject to the template. A: Manual identification of anatomical marker (one point in the spinal cord at C2–C3 vertebral level). B: Automatic reconstruction of the spinal cord centerline. C: Spinal cord straightening using thin-plate spline interpolation. D: Registration to the template and warping back data to the native space (here labeling of vertebral level).

slight subject motion between scans and distortions in EPI data). All transformations (affine and non-rigid) were then concatenated to produce a single transformation, which was subsequently applied to the template objects (e.g., white and gray matter atlases, as shown in the figure).

Despite the different contrasts and levels of distortions across sequences, all images were successfully registered to the template, as assessed qualitatively. The red grid overlaid on images enables to

appreciate the spatial correspondence within each sequence (between native and template), and the slight deformation/motion between sequences. The use of mutual information criterion for registration with SyN deformation ensured robustness and fast convergence of images with very different contrasts, such as the T<sub>1</sub>-weighted MPRAGE and the diffusion-weighted image. Such multi-modal registration is a first step towards automated and bias-free group analysis of multi-parametric MRI of the spinal cord.

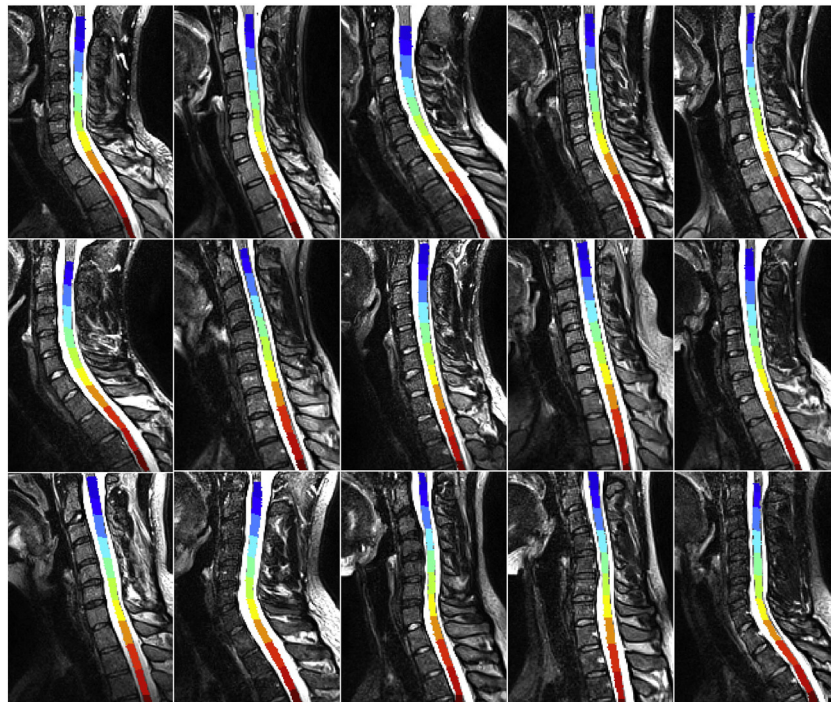


**Fig. 4.** Results of registration, evaluated by warping the template labels onto the native data for each of the fifteen subjects (other than the ones used to generate the template). Each panel shows the sagittal T<sub>2</sub>-weighted anatomical image, with an overlay of the warped spinal cord segmentation and labeling of vertebral level. In order to facilitate the visualization, volumes were “flattened” by straightening the spinal cord in the R–L direction, using information from the centerline. Note that in some subjects, the vertebral labeling does not appear orthogonal to the spinal cord, which is due to the nearest neighbor interpolation used to bring the label into the subject’s native space.

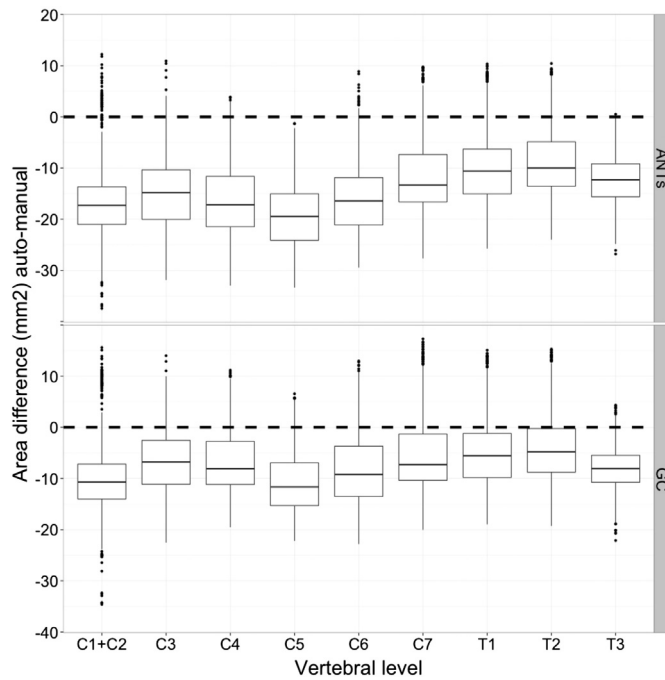


**Fig. 5.** Difference (in  $\text{mm}^2$ ) between the estimated spinal cord cross-section area and manual results. “ANTs” corresponds to the results after non-linear registration and warping and “GC” corresponds to the final results obtained after graph-cut segmentation. The box plots represent the median (horizontal line in the middle), the 25–75 percentiles (edge of the box), the 5–95 percentiles (vertical lines) and outliers (dots).

## Discussion

This paper presented a framework to produce an unbiased average anatomical template of the human spinal cord: MNI-Poly-AMU. It also described an image processing pipeline to register new subjects to the template that requires only one simple manual intervention to identify a single landmark that is used to vertically align the spinal

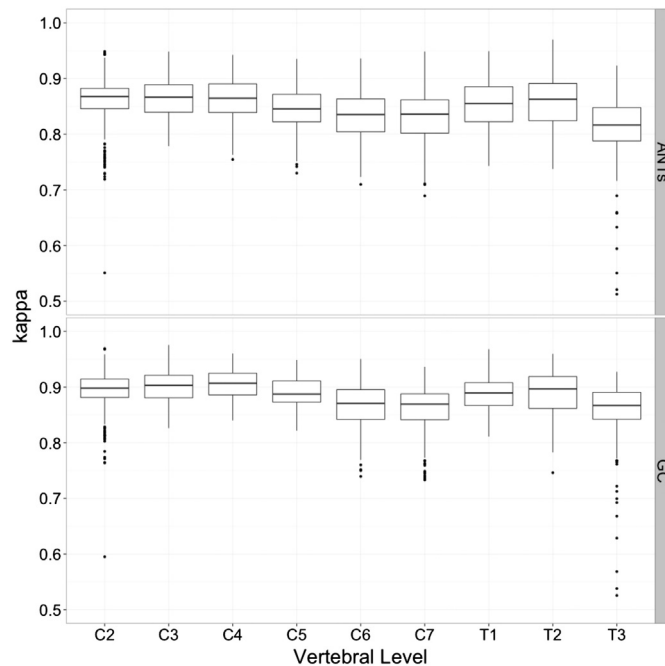


**Fig. 6.** 2D Dice overlap between manual and automatic segmentation results. “ANTs” corresponds to the results after non-linear registration and warping and “GC” corresponds to the final results obtained after graph-cut segmentation.

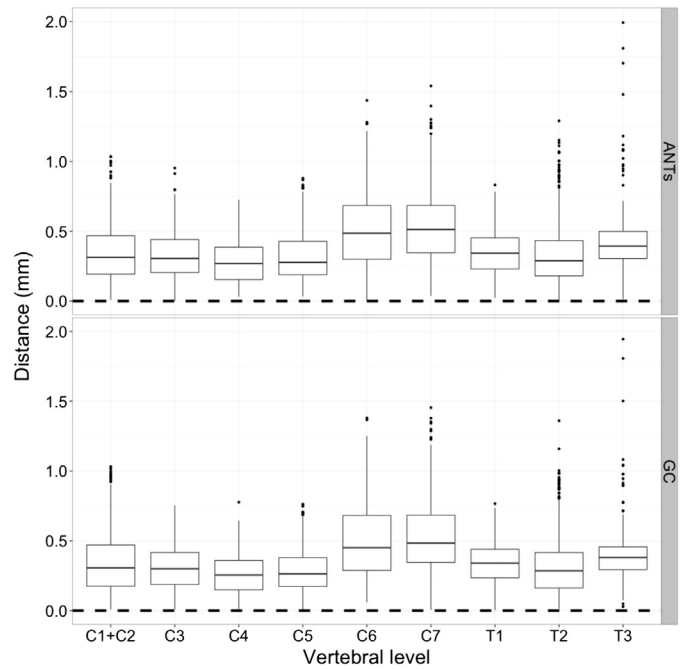


**Fig. 7.** Absolute in-plane distance (in mm) between centers-of-mass of segmented spinal cord and the manually segmented one. “ANTs” corresponds to the results after non-linear registration and warping and “GC” corresponds to the final results obtained after graph-cut segmentation.

cords. The procedure is rapid, robust and reduces bias associated with manual processing.

## Unbiased template creation and registration pipeline

While several studies have proposed methods to create a spinal cord template, most of these studies were based on the arbitrary selection of a reference subject for non-linear registration of other subjects to it (Eippert et al., 2009; Tozer et al., 2012). This can introduce a bias in the final template, as some morphological features (e.g., spinal cord position within the spinal canal, cross-sectional area, length, curvature) do not represent the average morphology, and hence subsequent registration would be prone to lower robustness and potentially larger errors. Here, the proposed framework produces an unbiased average anatomical template of the human spinal cord, because it iteratively constructs the template using the information from all input subjects. The non-rigid registration algorithm used to create the template is based on the symmetric image normalization (SyN) method implemented in ANTs (Avants et al., 2008) and was ranked the top registration procedure in a comparative study of nonlinear registration methods (Klein et al., 2009). This method ensures the recovered transformation to be diffeomorphic (satisfying the smoothness, bijective and invertible), criteria required for building a template. A similar template creation procedure has been used for the brain (Fonov et al., 2011), basal ganglia and deep brain structures (Haegelen et al., 2013) and cerebellum (Weier et al., 2014). While the current study only used 16 subjects to generate the template, the same method can be applied to a larger population. This will be the subject of future investigation.

In addition to the template creation, this paper proposed a semi-automatic image processing pipeline that can be used to register new subjects to the template. The overall procedure consists of (i) manually identifying a single point at C2–C3 vertebral level followed by automatic steps for (ii) finding the spinal cord centerline, (iii) straightening the spinal cord, and (iv) registering the straightened spinal cord to the template. Hence, the only manual procedure is the identification of an anatomical landmark, which takes less than a minute. This procedure ensures robustness towards the registration of the spinal



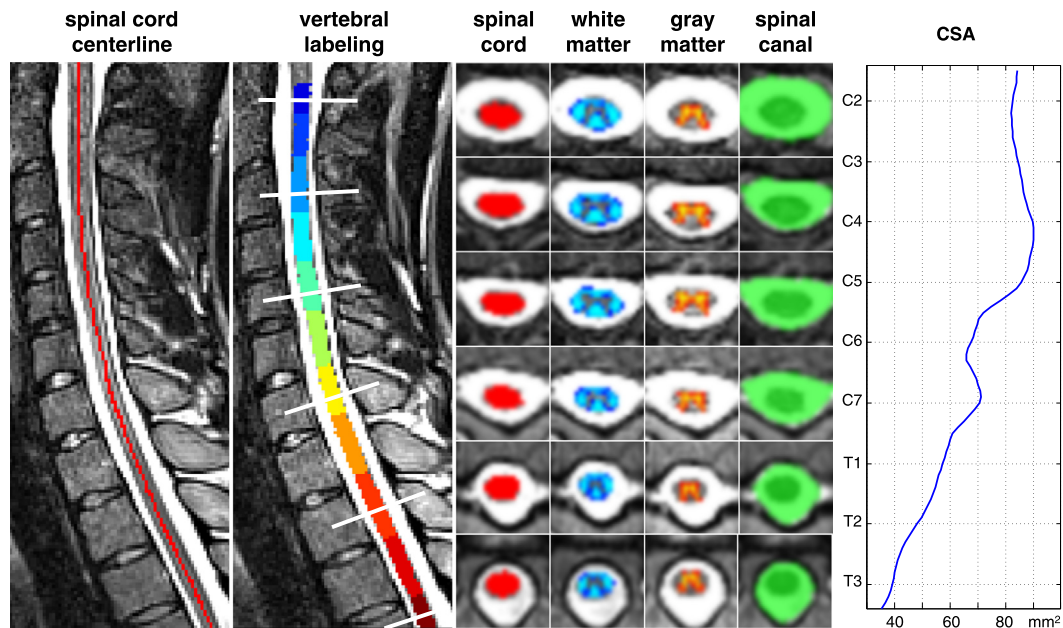


**Fig. 8.** Outputs of the template-based analysis: spinal cord centerline, labeling of vertebral levels, binary mask of the spinal cord, probabilistic masks of the white and gray matter, binary mask of the spinal canal and continuous measurements of cross sectional area (CSA) along the spinal cord. The white bars intersecting the cord on the sagittal image correspond to the selected axial views.

cord at the right vertebral levels, given the repetitive pattern of the vertebral bodies, which otherwise would cause mis-registration. The registration was validated in 15 new subjects acquired at another imaging center, and the median Dice coefficient against manual segmentation of the full spinal cord was 0.89. In an additional subject, other sequences were acquired to demonstrate the feasibility to register the template to data with different contrasts and levels of distortions than the template (see Fig. 9).

#### Limitations

One limitation of the current version of the MNI-Poly-AMU template is that it only covers C1 to T6 vertebral levels, preventing users from registering data below T6. Moreover, the template is based on a T<sub>2</sub>-weighted image and is therefore sub-optimal for registering T<sub>1</sub>-

weighted data (e.g., MPRAGE sequence). It should be mentioned however that registering T<sub>1</sub>-weighting data to the template is still possible, using mutual information metric for non-rigid deformation, or by inverting the image contrast. Also, the template is based on young adults (25–30 y.o.), and it has been shown that the morphology of the spinal cord (cross-sectional size, length and proportion of the cord in the spinal canal and ratio of gray and white matter volume) changes with age (Fradet et al., 2014; Kato et al., 2012). However, the non-rigid registration procedure ensures adaptability to different morphology, although this must be further tested in a wider population age in the future. The work presented here is a proof-of-concept to show that, in principle, the proposed framework can be applied to any vertebral level, image contrast and population age. A future version of the MNI-Poly-AMU template will include the brainstem and full spinal cord in T<sub>1</sub>- and T<sub>2</sub>-weighted contrasts. Moreover, any researcher can produce

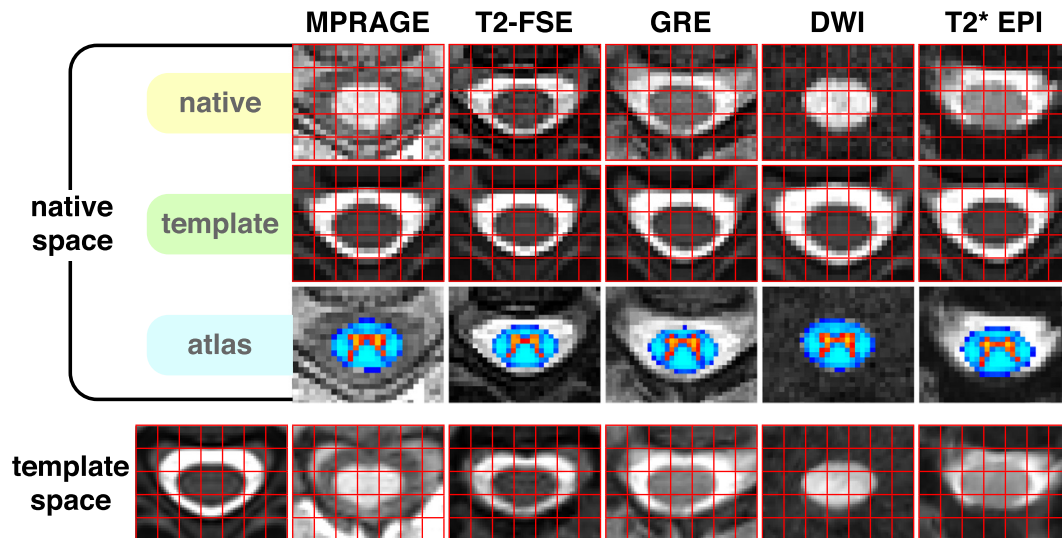


**Fig. 9.** Multi-parametric registration to the template. Images are centered at C2 vertebral level. The first group or three lines (native space) include the image in the native space (native), the registered template (template) and the white and gray matter atlas warped to the native space using the estimated transformation (atlas). The second main line shows all registered images in the template space. A red grid is overlaid to appreciate the inter-modality distortions and the accuracy of template registration within each sequence.

their age-specific template using these techniques and publically available software, e.g. for studying pediatric population (Mulcahey et al., 2012).

CSA was under-estimated by 16%. This under-estimation of CSA could be attributed to the slightly darker contour of the  $T_2$ -weighted image, accentuating partial volume effects with the surrounding CSF (El Mendili et al., 2014). Using the MPRAGE sequence, over-estimation of 14% was observed using the active contour method (Horsfield et al., 2010) and under-estimation of 4.5% using a semi-automatic contour detection method (Losseff et al., 1996). Sensitivity of image contrast to CSA measures has already been reported in a study comparing  $T_2$ -weighted SPACE and  $T_1$ -weighted MPRAGE sequences (De Leener et al., in press) and in another study comparing  $T_1$ -weighted MPRAGE (3D-TFE) and 3D phase sensitive inversion recovery (PSIR) sequences (Kearney et al., 2014). Discrepancies in CSA measures between sequences can be caused by differences in CSF/cord contrast,  $T_2^*$  blurring, Gibbs, motion and flow artifacts. These differences would thus change the appreciation of the cord boundaries by the user (in case of manual segmentation) or by the algorithm (in case of automated segmentation). It is worth noting that the type of MRI contrast can also impact the physical appearance of the boundaries. For example, the dura mater has a relatively short  $T_2^*$  value and hence its apparent location varies with the choice of TE in gradient echo sequences (Fujimoto et al., 2014). Moreover, age-related increase of iron deposition in the dura mater would be another factor of CSA under-estimation caused by  $T_2^*$  reduction, which can be a confounding factor in longitudinal studies.

#### Applications and perspectives

The outputs of the registration pipeline include two warping fields: one to register the template to the subject's anatomical data (forward) and the other to register the subject's anatomical data to the template (backward). Moreover, other useful data associated with the template are provided in the subject's anatomical space, such as spinal cord and CSF binary masks, white and gray matter probabilistic masks and labeling of vertebral level. For example, the CSF mask can be used to estimate a physiological noise regressor in fMRI experiments (Brooks et al., 2008), which otherwise has to be performed manually.

The probabilistic white matter template, once registered to the subject's space, represents useful information to automatically quantify multi-parametric data sensitive to white matter microstructure, such as DTI and magnetization transfer. Moreover, given that the white matter template is probabilistic, it is possible to weight quantitative values (e.g., from DTI data) based on the amount of partial volume effect, as previously suggested using fuzzy logic methods (Ellingson et al., 2007). Quantification of WM metrics using the proposed template has been demonstrated in a preliminary multi-center DTI study (Cohen-Adad et al., 2014b). Also, quantification of DTI metrics based on the WM/GM probabilistic template has been compared to manual delimitation of the white and gray matter in another preliminary study (Taso et al., 2014a).

In the current framework, the gray matter probabilistic boundary estimate provided with the MNI-Poly-AMU template is warped onto the subject's space using the deformation estimated from the  $T_2$ -weighted volume, and hence does not represent the subject's exact gray matter contour. As mentioned previously, the size and shape of the gray matter vary across individuals (Fradet et al., 2014). Notably, the proportion of gray/white matter decreases with age and the width of the posterior horns varies with gender. A preliminary use of the GM template has been proposed to investigate gray matter atrophy in elderly people using voxel based morphometry (Taso et al., 2014a). Despite this variability, mapping the gray matter probabilistic contour can be useful for several purposes. For example, it can be used as an initial step for automatic segmentation methods (Asman et al., 2014; Asman et al., 2013). It can also be used to produce an atlas-based parcellation of the spinal

cord gray matter into functional units, which would guide functional MRI experiments.

Labeling of vertebral levels is another feature provided by the template. This information can be used to report level-specific values of CSA along the spine. Having access to vertebral labeling under a quasi-automated framework opens the door to large-scale group studies, focusing on understanding the pathophysiology of diseases by looking at the evolution of CSA at specific vertebral levels, such as in MS (Klein et al., 2011; Valsasina et al., 2012) or in ALS (Cohen-Adad et al., 2013). In future work, we will evaluate the robustness of the pipeline to pathological data in different diseases. In addition, vertebral level information can be coupled with multi-parametric data, obtained from DTI or magnetization transfer imaging, to obtain normative values along the spine (Ellingson et al., 2008; Smith et al., 2010). Similarly to CSA, these level-specific normative data can be used to assess the state of individual patients or to evaluate the efficacy of new treatments. Finally, knowing the location of vertebral levels is useful to infer the location of the spinal levels (nerve rootlet entries), which are otherwise difficult to observe in standard anatomical scans. Knowing the location of spinal levels is particularly useful for fMRI experiments, in order to assess task-related activations or to perform group analysis. It should however be mentioned that the position of the nerve rootlets relative to the corresponding vertebral level can vary across individuals, as been shown by Cadotte et al. (2014) where the authors built a probabilistic map of nerve rootlet location based on vertebral levels. Hence, an exciting avenue would be to integrate this probabilistic map into the proposed template.

#### Conclusion

This paper presented an unbiased average anatomical template of the human spinal cord, as well as a quasi-automatic image processing pipeline that registers new subjects to the template. The template can notably be used for measurements of spinal cord cross-sectional area, voxel-based morphometry, identification of anatomical features (e.g., vertebral levels, white and gray matter location) and unbiased extraction of multi-parametric data. The MNI-Poly-AMU template and image processing software are freely available for MINC (<http://www.bic.mni.mcgill.ca/ServicesAtlases>) and for NIFTI file format (<http://sourceforge.net/projects/spinalcordtoolbox/>).

#### Acknowledgments

The authors thank Kevin Nigaud (CENIR), Carolyn Hurst and André Cyr (CRIUGM) for assistance with MRI acquisitions. This study was supported by the Association Française contre les Myopathies (AFM), the Institut pour la Recherche sur la Moelle épinière et l'Encéphale (IRME), the SensoriMotor Rehabilitation Research Team of the Canadian Institute of Health Research, the National MS Society [FG1892A1/1], the Fonds de Recherche du Québec-Santé, the Quebec BioImaging Network and the Natural Sciences and Engineering Research Council of Canada and the French National Research Agency ("Investissements d'Avenir", A\*MIDEX project no. ANR-11-IDEX-0001-02).

#### References

- Asman, A.J., Smith, S.A., Reich, D.S., Landman, B.A., 2013. Robust GM/WM segmentation of the spinal cord with iterative non-local statistical fusion. *Med. Image Comput. Comput. Assist. Interv.* 16, 759–767.
- Asman, A.J., Bryan, F.W., Smith, S.A., Reich, D.S., Landman, B.A., 2014. Groupwise multi-atlas segmentation of the spinal cord's internal structure. *Med. Image Anal.* 18, 460–471.
- Avants, B.B., Epstein, C.L., Grossman, M., Gee, J.C., 2008. Symmetric diffeomorphic image registration with cross-correlation: evaluating automated labeling of elderly and neurodegenerative brain. *Med. Image Anal.* 12, 26–41.
- Boykov, Y., Funka-Lea, G., 2006. Graph cuts and efficient N-D image segmentation. *Int. J. Comput. Vis.* 70, 109–131.

- Brooks, J.C., Beckmann, C.F., Miller, K.L., Wise, R.G., Porro, C.A., Tracey, I., Jenkinson, M., 2008. Physiological noise modelling for spinal functional magnetic resonance imaging studies. *NeuroImage* 39, 680–692.
- Cadotte, D.W., Cadotte, A., Cohen-Adad, J., Fleet, D., Livne, M., Mikulis, D., Fehlings, M.G., 2014. Resolving the anatomic variability of the human cervical spinal cord: a solution to facilitate advanced neural imaging. *Proceedings of the 22nd Annual Meeting of ISMRM*, Milan, Italy, p. 1719.
- Chen, M., Carass, A., Oh, J., Nair, G., Pham, D.L., Reich, D.S., Prince, J.L., 2013. Automatic magnetic resonance spinal cord segmentation with topology constraints for variable fields of view. *NeuroImage* 83, 1051–1062.
- Cohen-Adad, J., El Mendili, M.-M., Lehericy, S., Pradat, P.-F., Blanche, S., Rossignol, S., Benali, H., 2011a. Demyelination and degeneration in the injured human spinal cord detected with diffusion and magnetization transfer MRI. *NeuroImage* 55, 1024–1033.
- Cohen-Adad, J., Mareyam, A., Keil, B., Polimeni, J.R., Wald, L.L., 2011b. 32-channel RF coil optimized for brain and cervical spinal cord at 3 T. *Magn. Reson. Med.* 66, 1198–1208.
- Cohen-Adad, J., El Mendili, M.M., Morizot-Koutlidis, R., Lehericy, S., Meininger, V., Blanche, S., Rossignol, S., Benali, H., Pradat, P.F., 2013. Involvement of spinal sensory pathway in ALS and specificity of cord atrophy to lower motor neuron degeneration. *Amyotroph. Lateral Scler. Frontotemporal Degener.* 14, 30–38.
- Cohen-Adad, J., De Leener, B., Benhamou, M., Cadotte, D., Fleet, D., Cadotte, A., Fehlings, M. G., Pelletier Paquette, J.P., Thong, W., Taso, M., Collins, D.L., Callot, V., Fonov, V., 2014a. Spinal Cord Toolbox: an open-source framework for processing spinal cord MRI data. *Proceedings of the 20th Annual Meeting of OHBM*, Hamburg, Germany, p. 3633.
- Cohen-Adad, J., Samson, R.S., Schneider, T., Smith, A.K., Benhamou, M., Leveque, G., Smith, S.A., Wheeler-Kingshott, C.A.M., 2014b. Multisite DTI of the spinal cord with integrated template and white matter atlas processing pipeline. *Proceedings of the 22nd Annual Meeting of ISMRM*, Milan, Italy, p. 1727.
- Collins, D.L., Neelin, P., Peters, T.M., Evans, A.C., 1994. Automatic 3D intersubject registration of MR volumetric data in standardized Talairach space. *J. Comput. Assist. Tomogr.* 18, 192–205.
- Collins, D.L., Holmes, C.J., Peters, T.M., Evans, A.C., 1995. Automatic 3-D model-based neuroanatomical segmentation. *Hum. Brain Mapp.* 3, 190–208.
- De Leener, B., Kadoury, S., Cohen-Adad, J., 2014. Robust, accurate and fast automatic segmentation of the spinal cord. *NeuroImage* 98, 528–536.
- Dice, L.R., 1945. Measures of the amount of ecologic associations between species. *J. Ecol.* 26, 297–302.
- Dowell, N.G., Jenkins, T.M., Ciccarelli, O., Miller, D.H., Wheeler-Kingshott, C.A., 2009. Contiguous-slice zonally oblique multislice (CO-ZOOM) diffusion tensor imaging: examples of in vivo spinal cord and optic nerve applications. *J. Magn. Reson. Imaging* 29, 454–460.
- Eippert, F., Finsterbusch, J., Bingel, U., Büchel, C., 2009. Direct evidence for spinal cord involvement in placebo analgesia. *Science* 326, 404.
- El Mendili, M.M., Chen, R., Tret, B., Pellegrini-Issac, M., Cohen-Adad, J., Lehericy, S., Pradat, P.F., Benali, H., 2014. Validation of a semiautomated spinal cord segmentation method. *J. Magn. Reson. Imaging* <http://dx.doi.org/10.1002/jmri.24571>.
- Ellingson, B.M., Ulmer, J.L., Schmit, B.D., 2007. Gray and white matter delineation in the human spinal cord using diffusion tensor imaging and fuzzy logic. *Acad. Radiol.* 14, 847–858.
- Ellingson, B.M., Ulmer, J.L., Kurpad, S.N., Schmit, B.D., 2008. Diffusion tensor MR imaging of the neurologically intact human spinal cord. *AJNR Am. J. Neuroradiol.* 29, 1279–1284.
- Finsterbusch, J., 2009. High-resolution diffusion tensor imaging with inner field-of-view EPI. *J. Magn. Reson. Imaging* 29, 987–993.
- Finsterbusch, J., Eippert, F., Büchel, C., 2012. Single, slice-specific z-shim gradient pulses improve T2\*-weighted imaging of the spinal cord. *NeuroImage* 59, 2307–2315.
- Fonov, V., Evans, A.C., Botteron, K., Almli, C.R., McKinstry, R.C., Collins, D.L., 2011. Unbiased average age-appropriate atlases for pediatric studies. *NeuroImage* 54, 313–327.
- Fradet, L., Arnoux, P.J., Ranjeva, J.P., Petit, Y., Callot, V., 2014. Morphometrics of the entire human spinal cord and spinal canal measured from in vivo high-resolution anatomical magnetic resonance imaging. *Spine (Phila Pa 1976)* 39, E262–E269.
- Fujimoto, K., Polimeni, J.R., van der Kouwe, A.J., Reuter, M., Kober, T., Benner, T., Fischl, B., Wald, L.L., 2014. Quantitative comparison of cortical surface reconstructions from MP2RAGE and multi-echo MPRAGE data at 3 and 7 T. *NeuroImage* 90, 60–73.
- Haegelen, C., Coupe, P., Fonov, V., Guizard, N., Jannin, P., Morandi, X., Collins, D.L., 2013. Automated segmentation of basal ganglia and deep brain structures in MRI of Parkinson's disease. *Int. J. Comput. Assist. Radiol. Surg.* 8, 99–110.
- Horsfield, M.A., Sala, S., Neema, M., Absinta, M., Bakshi, A., Sormani, M.P., Rocca, M.A., Bakshi, R., Filippi, M., 2010. Rapid semi-automatic segmentation of the spinal cord from magnetic resonance images: application in multiple sclerosis. *NeuroImage* 50, 446–455.
- Huber, P., Ronchetti, E., 2009. *Robust Statistics*, 2nd edition. Wiley.
- Jenkinson, M., Bannister, P., Brady, M., Smith, S., 2002. Improved optimization for the robust and accurate linear registration and motion correction of brain images. *NeuroImage* 17, 825–841.
- Kato, F., Yukawa, Y., Suda, K., Yamagata, M., Ueta, T., 2012. Normal morphology, age-related changes and abnormal findings of the cervical spine. Part II: magnetic resonance imaging of over 1,200 asymptomatic subjects. *Eur. Spine J.* 21, 1499–1507.
- Kearney, H., Yiannakas, M.C., Abdel-Aziz, K., Wheeler-Kingshott, C.A., Altmann, D.R., Ciccarelli, O., Miller, D.H., 2014. Improved MRI quantification of spinal cord atrophy in multiple sclerosis. *J. Magn. Reson. Imaging* 39, 617–623.
- Klein, A., Andersson, J., Ardekani, B.A., Ashburner, J., Avants, B., Chiang, M.C., Christensen, G.E., Collins, D.L., Gee, J., Hellier, P., Song, J.H., Jenkinson, M., Lepage, C., Rueckert, D., Thompson, P., Vercauteren, T., Woods, R.P., Mann, J.J., Parsey, R.V., 2009. Evaluation of 14 nonlinear deformation algorithms applied to human brain MRI registration. *NeuroImage* 46, 786–802.
- Klein, J.P., Arora, A., Neema, M., Healy, B.C., Tauhid, S., Goldberg-Zimring, D., Chavarro-Nieto, C., Stankiewicz, J.M., Cohen, A.B., Buckle, G.J., Houtchens, M.K., Ciccarelli, A., Dell'Oglio, E., Guttmann, C.R., Alsop, D.C., Hackney, D.B., Bakshi, R., 2011. A 3 T MR imaging investigation of the topography of whole spinal cord atrophy in multiple sclerosis. *AJNR Am. J. Neuroradiol.* 32, 1138–1142.
- Lang, J., 1993. *Clinical Anatomy of the Cervical Spine*. Thieme Medical Publishers, New York.
- Losseff, N.A., Webb, S.L., O'Riordan, J.L., Page, R., Wang, L., Barker, G.J., Tofts, P.S., McDonald, W.I., Miller, D.H., Thompson, A.J., 1996. Spinal cord atrophy and disability in multiple sclerosis. A new reproducible and sensitive MRI method with potential to monitor disease progression. *Brain* 119 (Pt 3), 701–708.
- Manjon, J.V., Coupe, P., Martí-Bonmati, L., Collins, D.L., Robles, M., 2010. Adaptive non-local means denoising of MR images with spatially varying noise levels. *J. Magn. Reson. Imaging* 31, 192–203.
- Mulcahey, M.J., Samdani, A., Gaughan, J., Barakat, N., Faro, S., Betz, R.R., Finsterbusch, J., Mohamed, F.B., 2012. Diffusion tensor imaging in pediatric spinal cord injury: preliminary examination of reliability and clinical correlation. *Spine (Phila Pa 1976)* 37, E797–E803.
- Sigmund, E.E., Suero, G.A., Hu, C., McGorty, K., Sodickson, D.K., Wiggins, G.C., Helpert, J.A., 2012. High-resolution human cervical spinal cord imaging at 7 T. *NMR Biomed.* 25, 891–899.
- Smith, S.A., Jones, C.K., Gifford, A., Belegu, V., Chodkowski, B., Farrell, J.A.D., Landman, B.A., Reich, D.S., Calabresi, P.A., McDonald, J.W., Van Zijl, P.C.M., 2010. Reproducibility of tract-specific magnetization transfer and diffusion tensor imaging in the cervical spinal cord at 3 Tesla. *NMR Biomed.* 23, 207–217.
- Stroman, P.W., Figley, C.R., Cahill, C.M., 2008. Spatial normalization, bulk motion correction and coregistration for functional magnetic resonance imaging of the human cervical spinal cord and brainstem. *Magn. Reson. Imaging* 26, 809–814.
- Stroman, P.W., Bosma, R.L., Tsyben, A., 2012. Somatotopic arrangement of thermal sensory regions in the healthy human spinal cord determined by means of spinal cord functional MRI. *Magn. Reson. Med.* 68, 923–931.
- Stroman, P.W., Wheeler-Kingshott, C., Bacon, M., Schwab, J.M., Bosma, R., Brooks, J., Cadotte, D., Carlstedt, T., Ciccarelli, O., Cohen-Adad, J., Curt, A., Evangelou, N., Fehlings, M.G., Filippi, M., Kelley, B.J., Kollias, S., Mackay, A., Porro, C.A., Smith, S., Strittmatter, S.M., Summers, P., Tracey, I., 2014. The current state-of-the-art of spinal cord imaging: methods. *NeuroImage* 84, 1070–1081.
- Taso, M., Le Troter, A., Sdika, M., Ranjeva, J.P., Guye, M., Bernard, M., Callot, V., 2014a. Construction of an in vivo human spinal cord atlas based on high-resolution MR images at cervical and thoracic levels: preliminary results. *MAGMA* 27, 257–267.
- Taso, M., Le Troter, A., Sdika, M., Fonov, V.S., Cohen-Adad, J., Guye, M., Ranjeva, J.P., Callot, V., 2014b. Validation of a 2D spinal cord probabilistic atlas. Application to FA measurement and VBM study of the GM atrophy occurring with age. *Proceedings of the 22nd Annual Meeting of ISMRM*, Milan, Italy, p. 1710.
- Tozer, D., Yiannakas, M.C., Kearney, H., Wheeler-Kingshott, C.A.M., 2012. Cervical spinal cord template of healthy controls using high-resolution axial gradient echo imaging. *Proceedings of the 20th Annual Meeting of ISMRM*, Melbourne, Australia, p. 1043.
- Tustison, N.J., Avants, B.B., Cook, P.A., Zheng, Y., Egan, A., Yushkevich, P.A., Gee, J.C., 2010. N4ITK: improved N3 bias correction. *IEEE Trans. Med. Imaging* 29, 1310–1320.
- Valsasina, P., Horsfield, M.A., Rocca, M.A., Absinta, M., Comi, G., Filippi, M., 2012. Spatial normalization and regional assessment of cord atrophy: voxel-based analysis of cervical cord 3D T1-weighted images. *Am. J. Neuroradiol.* 33, 2195–2200.
- Weier, K., Fonov, V., Lavoie, K., Doyon, J., Collins, D.L., 2014. Rapid automatic segmentation of the human cerebellum and its lobules (RASCAL)—implementation and application of the patch-based label-fusion technique with a template library to segment the human cerebellum. *Hum. Brain Mapp.* <http://dx.doi.org/10.1002/hbm.22529>.
- Wheeler-Kingshott, C.A., Stroman, P.W., Schwab, J.M., Bacon, M., Bosma, R., Brooks, J., Cadotte, D.W., Carlstedt, T., Ciccarelli, O., Cohen-Adad, J., Curt, A., Evangelou, N., Fehlings, M.G., Filippi, M., Kelley, B.J., Kollias, S., Mackay, A., Porro, C.A., Smith, S., Strittmatter, S.M., Summers, P., Thompson, A.J., Tracey, I., 2014. The current state-of-the-art of spinal cord imaging: applications. *NeuroImage* 84, 1082–1093.
- Yiannakas, M.C., Kearney, H., Samson, R.S., Chard, D.T., Ciccarelli, O., Miller, D.H., Wheeler-Kingshott, C.A.M., 2012. Feasibility of grey matter and white matter segmentation of the upper cervical cord in vivo: a pilot study with application to magnetisation transfer measurements. *NeuroImage* 63, 1054–1059.